A Study on the Flow around a Strut Mounted on a Plate with an Angle of Attack

by Sun-Young Kim*, *Member* Kazu-hiro Mori*, *Member*

Summary

A computational and experimental study on the flow around the strut-plate juncture with zero and 5° angle of attack is presented to make clear its flow characteristics. The separation lines on the surface of the plate and the strut being visualized, the flows are simulated by solving the Navier-Stokes equations for the two Reynolds numbers, 10^3 and 10^4. The computational results seem to agree with the visualized flows qualitatively. Characteristics of the junction flow are discussed by making use of the computational results. It is made clear that the effects of the Reynolds number and the angle of attack on the flow are noticeable. The estimated pressure and skin friction on the strut showed a strong three-dimensionality in spanwise. It can be concluded that such numerical studies can be an effective tool for the study of complicated flow.

1. Introduction

When an oncoming boundary layer flow encounters a body mounted on the plate, the flow separates in front of the body due to the blocking effect. The separated flow forms several vortices depending on the flow conditions and they sweep around the body to generate horseshoe vortices and interact with the corner flow at the downstream. This flow is sometimes called junction flow and can be found in the juncture of the appendages attached to a ship hull.

The study of a junction flow is practically important because the generated horsesoe vortices greatly affect the resistance, the performance of the appendages and the other devices located downstream. Especially for high speed twin-screw ships with relatively large appendages, the increase of the resistance by appendages amounts to 20~30 % of the total resistance of the ship[1]. Although some systematic experimental studies are performed through conventional tank tests[2], the estimation of the resistance of the appendages meets with difficulty in the uncertainty of the scale effect. The basic understanding about the junction flow is required to cope with unconventional high-speed ships which may have new type appendages.

Most of the previous studies on the junction flow have been performed for a simple configuration of body and plate to understand the fundamental mechanism of the junction flow by simplifying the problem ; studies have been carried out to understand the structure of the horseshoe vortex on the surface of the circular cylinder and plate by flow visualization and pressure measurements[3,4,5]. Although detailed experimental measurements including velocities and turbulent intensities of the flow have been obtained to provide the data base for the study of junction flow[6,7,8,9], numerical simulation is indispensable for the further understanding. Numerical studies of the junction flow by the solution of the Navier-Stokes equations have been also carried out for the laminar[10] and turbulent[11,12] junction flows.

All of the above studies, however, have been for the zero angle of incidence except Briely et al.[13] where the flow only near the leading edge is computed for the 5° angle of attack. The study on the effects of the inflow angle on the junction flow is important as most of the appendages in application lies in the flow with some incidence angle.

The present study is initiated to make clear the flow mechanism of the junction flow both by numerical simulation and experiments where the effects of the angle of attack or inclination of the strut and the curvature of the plate on the flow and drag will be investigated.

In this paper, as a first step, a laminar junction flow around a strut mounted on the flat plate with/without angle of attack is investigated by making use of the numerical solutions of the Navier-Stokes equations. Flow visualizations are carried out in advance to grasp a general understanding of the flow. The numerical solutions have been obtained for the zero and $-5°$ incidence angle at two Reynolds numbers. The characteristics of the effects of the Reynolds number and the incidence angle on the junction flow are discussed. Other related experimental data are found in the reference[14].

* Faculty of Engineering, Hiroshima University

Received 10th JAN 1992
Read of the Spring meeting 12, 13th MAY 1992

2. Flow Visualization

An experimental study is carried out to have a general understanding about junction flows. Separation lines on the plate and strut were visualized by inputting a solution of powder and dye on the surfaces.

The profile of the strut section is shown in Table 1 whose chord length L and height are 40 cm and 1.2L respectively. The leading edge of the plate lies 1.9L upstream of that of the strut. Details on the experimental method and full data including pressure measurements can be found in the reference[14].

Fig. 1(a) shows the separation lines on the plate when the flow comes toward the strut with 5° angle of attack at the speed of 0.2 m/s; the Reynolds number R_n is about $8*10^4$. The black lines represent the place where the dye is accumulated. So they can be assumed as separation lines because the shear stresses are very small there. Two separation lines can be seen in this figure. The one wrapping around the strut is made because of the strong adverse pressure gradient in front of the strut and the other is a fish-tail-like line behind the strut which occurs due to the trailing edge separation. Due to the angle of attack the separation lines are unsymmetry. On the suction side, the former goes closer to the strut and the latter shifts to the direction of the trailing edge from the center line.

Fig. 1(b) shows the separation lines on the strut for the flow without angle of attack at the speed of 0.1 m/s. The separation delays around the top of the strut but occures earlier near the root compared with the middle part. High momentum supplied by the flow above the

Table 1 The Offset of the Section of the Strut

x/L (%)	0.0	10.0	20.0	30.0	40.0	50.0	60.0	70.0	80.0	90.0	100.
t/L (%)	0.00	10.5	14.2	16.5	17.4	17.8	17.4	16.0	12.4	7.8	0.9

L.E radius : 1.6%, (L: chord length, t: thicknes)

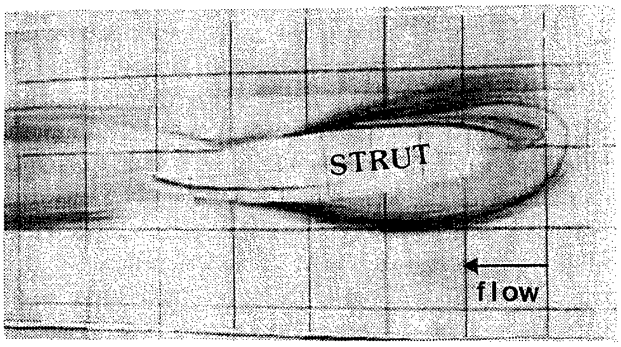

(a) On the Plate: $\alpha=5°$, $U=0.2$ m/s

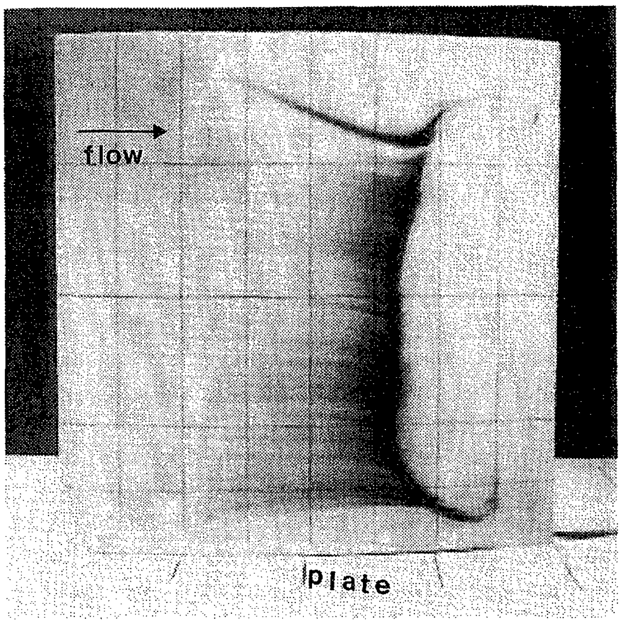

(c) On the Strut (suction side): $\alpha=5°$, $U=0.1$ m/s

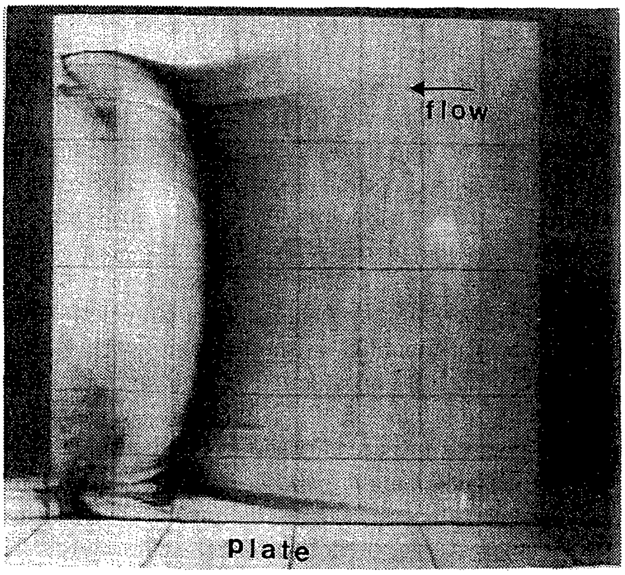

(b) On the Strut: $\alpha=0°$, $U=0.1$ m/s

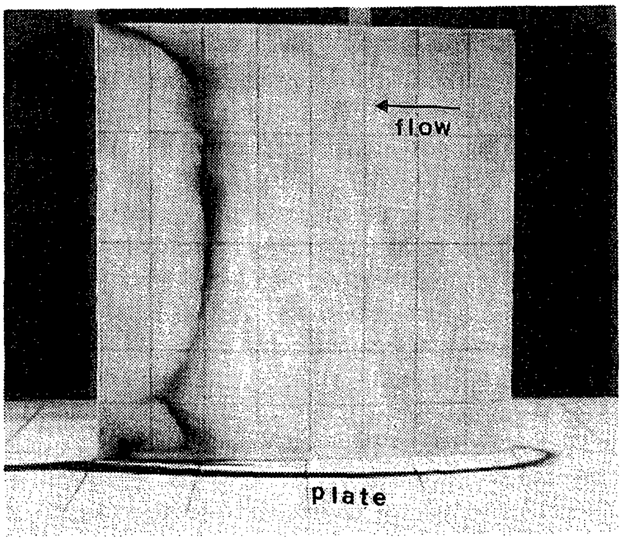

(d) On the Strut (pressure side): $\alpha=5°$, $U=0.1$ m/s

Fig. 1 The Results of Flow Visualization strut make the separation delayed around the top while the flow within boundary layer with lower momentum makes the flow separated earlier near the root. Another separation line near the juncture of the trailing edge and plate can be seen which is a result of strong back flow around the trailing edge. From this photograph, a longitudinal component of vortex is supposed to exist between these separatin lines.

Figs. 1(c) and 1(d) show the separation lines on the strut for the flow with 5° angle of attack at 0.1 m/s; Fig. 1(c) shows the suction side and Fig. 1(d) the pressure side. On the pressure side, the characteristics of the streamlines are generally similar to those without angle of attack shown in Fig. 1(b) but those on the suction side are different from others especially near the root where separation delays noticeably.

It can be understood from the results of the flow visualization that the behavior of the horseshoe vortex affects not only the flow on the plate but also the separation on the strut. However it is not easy to understand the structure of the inner flow precisely only from these experimental results. A numerical study parallel to the experiments seems indispensable for a sound understanding.

3. Computational Method

3.1 Governing Equation

The governing equations for the incompressible unsteady flow are given by the Navier-Stokes and continuity equations. They can be written in the nondimensinalized form as follows;

$$\begin{aligned} u_t+uu_x+vu_y+wu_z &= -p_x+\frac{1}{R_n}\nabla^2 u \\ v_t+uv_x+vv_y+wv_z &= -p_y+\frac{1}{R_n}\nabla^2 v \qquad (1) \\ w_t+uw_x+vw_y+ww_z &= -p_z+\frac{1}{R_n}\nabla^2 w \end{aligned}$$

$$u_x+v_y+w_z=0 \qquad (2)$$

where subscripts represent partial differentiations with respect to the referred variables and (u, v, w) and p are the velocity components in (x, y, z)-direction of the cartesian coordinates and the static pressure respectively. All the variables are nondimensionalized by the chord length of the strut L, the uniform flow velocity U_o and the density of water ρ. R_n is the Reynolds number based on U_o and L.

To represent the body accurately a body-fitted coordinate system is adopted and transformation is given by

$$\xi=\xi(x, y, z),\ \eta=\eta(x, y, z),\ \zeta=\zeta(x, y, z) \qquad (3)$$

With these relations, the following transformed governing equations are obtained.

$$\begin{aligned} u_t+Uu_\xi+Vu_\eta+Wu_\zeta &= -(\xi_x p_\xi+\eta_x p_\eta+\zeta_x p_\zeta)+\frac{1}{R_n}\nabla^2 u \\ v_t+Uv_\xi+Vv_\eta+Wv_\zeta &= -(\xi_y p_\xi+\eta_y p_n+\zeta_y p_\zeta)+\frac{1}{R_n}\nabla^2 v \\ w_t+Uw_\xi+Vw_\eta+Ww_\zeta &= -(\xi_z p_\xi+\eta_z p_\eta+\zeta_z p_\zeta)+\frac{1}{R_n}\nabla^2 w \qquad (4) \end{aligned}$$

$$\xi_x u_\xi+\eta_x u_\eta+\zeta_x u_\zeta+\xi_y v_\xi+\eta_y v_\eta+\zeta_y v_\zeta+\xi_z w_\xi+\eta_z w_\eta+\zeta_z w_\zeta=0 \qquad (5)$$

where U, V and W are the contravariant velocity components defined as

$$\begin{aligned} U&=\xi_x u+\xi_y v+\xi_z w \\ V&=\eta_x u+\eta_y v+\eta_z w \qquad (6) \\ W&=\zeta_x u+\zeta_y v+\zeta_z w \end{aligned}$$

Laplacian ∇^2 can be expressed in the body fitted coordinates as following form;

$$\begin{aligned} \nabla^2 q=&(\xi_x^2+\xi_y^2+\xi_z^2)q_{\xi\xi}+(\eta_x^2+\eta_y^2+\eta_z^2)q_{\eta\eta}+(\zeta_x^2+\zeta_y^2+\zeta_z^2)q_{\zeta\zeta} \\ &+2(\xi_x\eta_x+\xi_y\eta_y+\xi_z\eta_z)q_{\xi\eta}+2(\eta_x\zeta_x+\eta_y\zeta_y+\eta_z\zeta_z)q_{\eta\zeta}+2(\zeta_x\xi_x+\zeta_y\xi_y+\zeta_z\xi_z)q_{\zeta\xi} \\ &+(\xi_{xx}+\xi_{yy}+\xi_{zz})q_\xi+(\eta_{xx}+\eta_{yy}+\eta_{zz})q_\eta \\ &+(\zeta_{xx}+\zeta_{yy}+\zeta_{zz})q_\zeta \qquad (7) \end{aligned}$$

ξ_x, ξ_y and so on in Eqs. (4)-(7) are the metrics of the grid.

3.2 Numerical Scheme and Boundary Condition

MAC method[15,16] is employed for the computation where Poisson equation for the pressure is derived by taking a divergence of the momentum equation and satisfying the continuity equation. Relaxation method is used to solve the Poisson equation for the pressure and the velocities are updated from the momentum equation.

The finite difference equations are derived on the regular grid system. So all the variables are defined on the grid nodes. For the spatial differencing scheme, 2nd order central difference is used while 3rd-order upwind scheme for the convective term. Euler explicit scheme is used for the time marching procedure. Computation starts from the still state and the flow is accelerated up to the given constant velocity for the numerical stability.

C-type grid is adopted for the computation. The coordinate system and grid topology are shown in Fig. 2. In the physical domain, space-fixed cartesian coordinate system is used whose origin is located at the center of the strut on the plate and x-, y- and z- axes are in the uniform flow, lateral and vertical direction respectively.

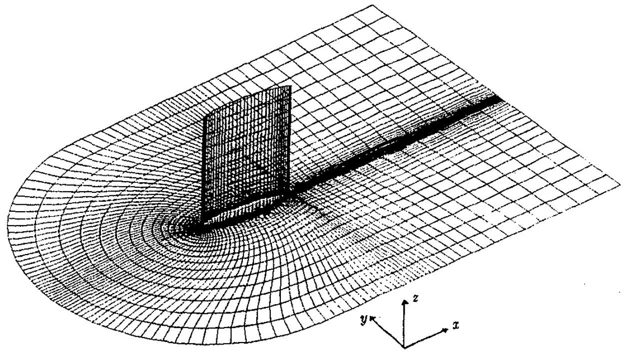

Fig. 2 Grid and Coordinate System

In the transformed body-fitted coordinate system, ξ- and η- axes are the girthwise of the strut and the normal-to the surface of strut and ζ-axis is the same with z-axis. Therefore the surface of the strut lies in the η-constant plane and the plate lies in the ζ-constant plane. The computation is made only for the half domain in case of zero angle of attack with the assumption of symmetric flow. So the grid topology for this case is different from the one for the full domain.

On the strut and flat plate, no-slip condition is used for the velocity and Neumann condition is obtained from the momentum equation for the pressure. Symmetric boundary conditions are applied on the symmetric planes by assuming that the flow is symmetric there.

Outer boundaries are taken on the plate including the inflow and the lateral boundaries where Blasius velocity profile with constant pressure is prescribed. When these boundaries are not far from the strut, the results may fall in wiggling solution near these boundaries. This problem can be improved to a extent by applying the zero-gradient condition only for the velocity component v[17]. The height of the strut is assumed to be infinite and the zero gradient conditions are used for all the variables. On the downstream boundary, the pressure is linearly extrapolated in the streamwise direction which means the diffusion of pressure in the streamwise direction is negligible.

3.3 Computational Condition

The profile of the strut section is the same as that used in experiments shown in Table 1. The leading edge of the plate is 3.5L apart from the center of the wing but infinite in lateral and downstream directions.

Two-dimensional C-type grids about the strut are generated by using a geometrical method[18] and three-dimensional grids are obtained by stacking them algebraically. Fig. 2 shows one of the grids used in computation.

The computing domain is as follows.

$$-2.3 \leq x \leq 3.0,\ -1.8 \leq y \leq 1.8,\ 0.0 \leq z \leq 1.2 \qquad (8)$$

The boundary layer thickness at the leading edge of the strut estimated from the Blasius solution is 0.274L and 0.0866L for $R_n=10^3$ and 10^4 respectively.
The computing conditions and grids for the three cases studied in this paper are summarized in Table 2.

The flow is accelerated until $t=1.0$ for all cases.

4. Results and Discussions

Computations of the flow with zero angle of attack are carried out at two Reynolds numbers, 10^3 and 10^4 while that with $-5°$ angle of attack is at $R_n=10^3$.

Convergence of the computation is checked by the maximum residual of the pressure and total forces acting on the strut. Fig. 3 shows the convergence history of the drag acting on the strut where C_d is the drag coefficient and C_{dp} and C_{df} are its pressure and frictional components respectively. For the low R_n computation, the convergence could be attained with sufficiently small error. However it takes a large computing time for the high R_n case because the development of the flow near the trailing edge is very slow although the flow in other regions has been converged already.

4.1 Junction Flow with Zero Angle of Attack

The computed upstream flow field and its vorticity contours on the plane of symmetry are shown in Figs. 4 and 5 for $R_n=10^3$ and $R_n=10^4$; the leading edge of the strut is at $x=-0.5$. Two kinds of a vortical flow are seen; a primary horseshoe vortex, positive in vorticity, and a counter-rotating secondary vortex confined to the corner region.

The boundary layer inflow to the strut induces a pressure gradient along the leading edge of the strut. Fig. 6 shows the distribution of the pressure coefficients on the leading edge. The pressure becomes constant above the boundary layer. The presence of the secondary vortex at the corner region can be verified by the peak of the pressure near the root ($z=0$) although it is not so clearly seen in the result at $R_n=10^3$, which may be attributed to insufficient resolution of grid. The pressure at $R_n=10^4$ is higher than at $R_n=10^3$ because the fluid with higher momentum is entrained into the secondary vortex region.

Fig. 7 shows the skin-friction coefficient C_f on the plate along the symmetry line. Two points where C_f is zero represent the separation and attachment points. The position of the attachment is closer to the strut at $R_n=10^4$ than that at $R_n=10^3$. This is because the flow with higher energy comes into the corner region and makes the separation of the downward flow delayed at

Table 2 Computing Conditions

Case		$\alpha=0°$ $R_n=10^3$	$\alpha=0°$ $R_n=10^4$	$\alpha=-5°$ $R_n=10^3$
Grids	number	57 * 27 * 20	65 * 32 * 30	113 * 27 * 20
	min. spacing	0.004	0.0004	0.004
time increment		0.002	0.0004	0.002
b.l thickness		0.2739	0.0866	0.2739
momentum thickness		0.0364	0.0115	0.0364

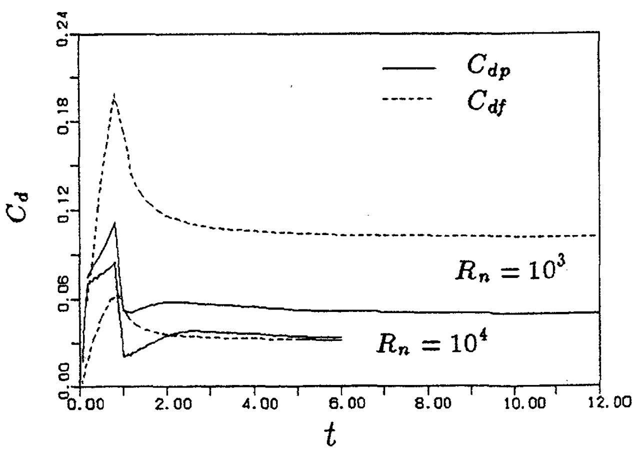

Fig. 3 Convergence History of the Forces acting on the Strut

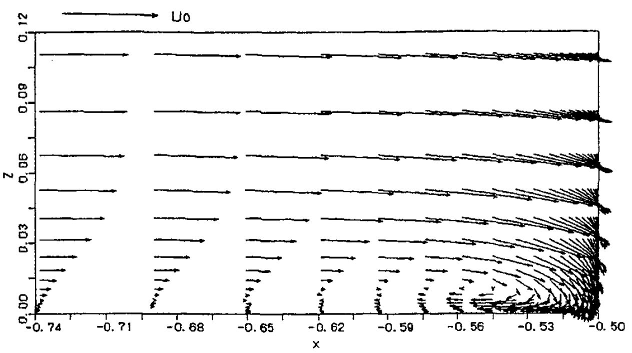

(a) Velocity Fields

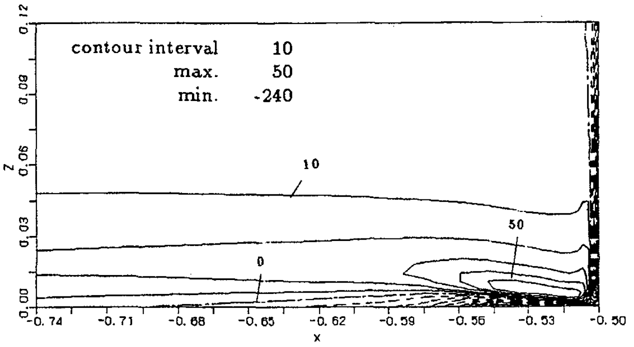

(b) y-component Vorticity Contours
(broken lines denote negative values)

Fig. 4 Flow at the Plane of Symmetry (upstream) : $R_n = 10^4$

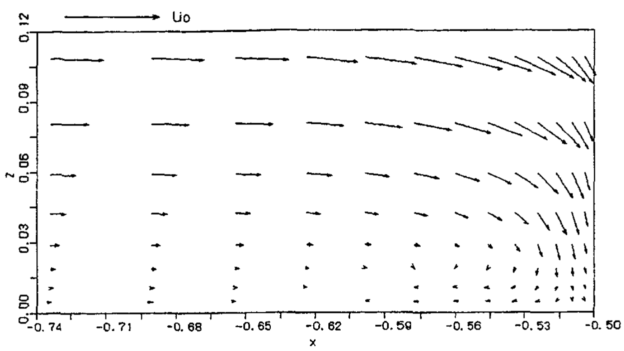

(a) Velocity Fields

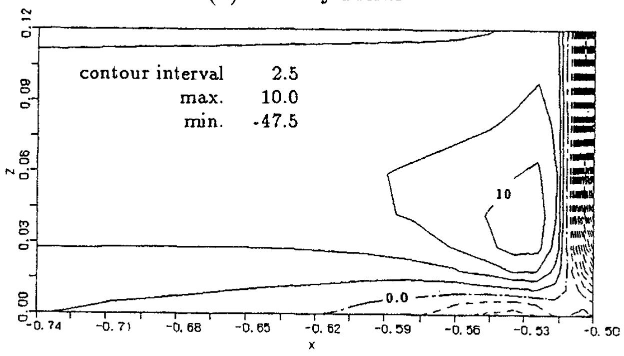

(b) y-component Vorticity Contours
(broken lines denote negative values)

Fig. 5 Flow at the Plane of Symmetry (upstream) : $R_n = 10^3$

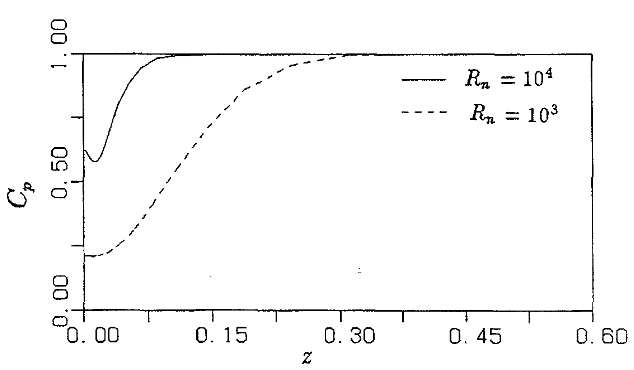

Fig. 6 Pressure on the Leading Edge of the Strut : $\alpha=0°$

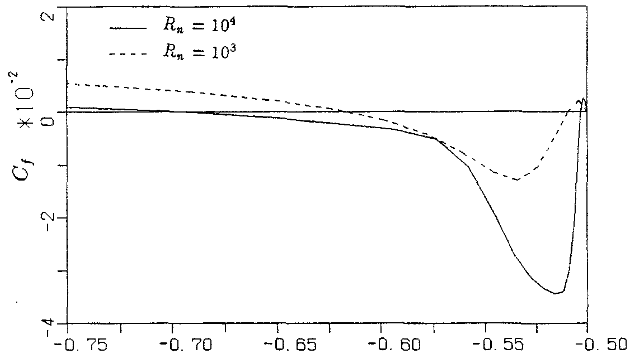

Fig. 7 Skin-Friction on the Plate along the Line of Symmetry (Upstream) : $\alpha=0°$

the leading edge. On the other hand, the separation occurs earier in the upstream for $R_n=10^4$. So the primary horseshoe vortex for $R_n=10^4$ has a more elongated shape as can be seen in Figs. 4 and 5.

Fig. 8 shows the pressure distribution on the plate along the symmetry line. It can be seen that the pressure is dropped in the vicinity of the leading edge and around $x=-0.55$ for $R_n=10^4$ where horseshoe vortex has been observed ; this is because the flow is accelerated by the vortex there.

Fig. 9 shows the cross-flow velocity and the contours of the streamwise velocity at several planes orthogonal to the surface of the strut or the plane of symmetry in the wake. The cross-flow and the streamwise velocity

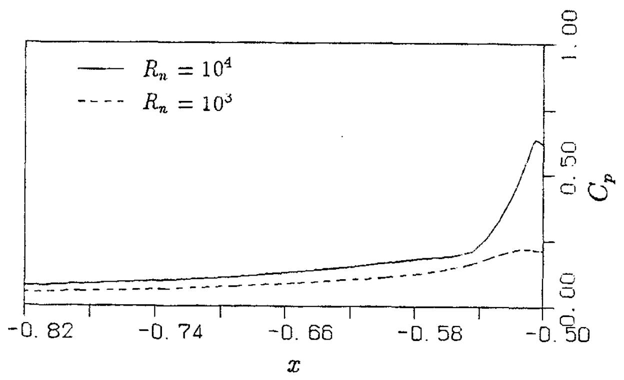

Fig. 8 Pressure on the Plate along the Line of Symmetry (Upstream) : $\alpha=0°$

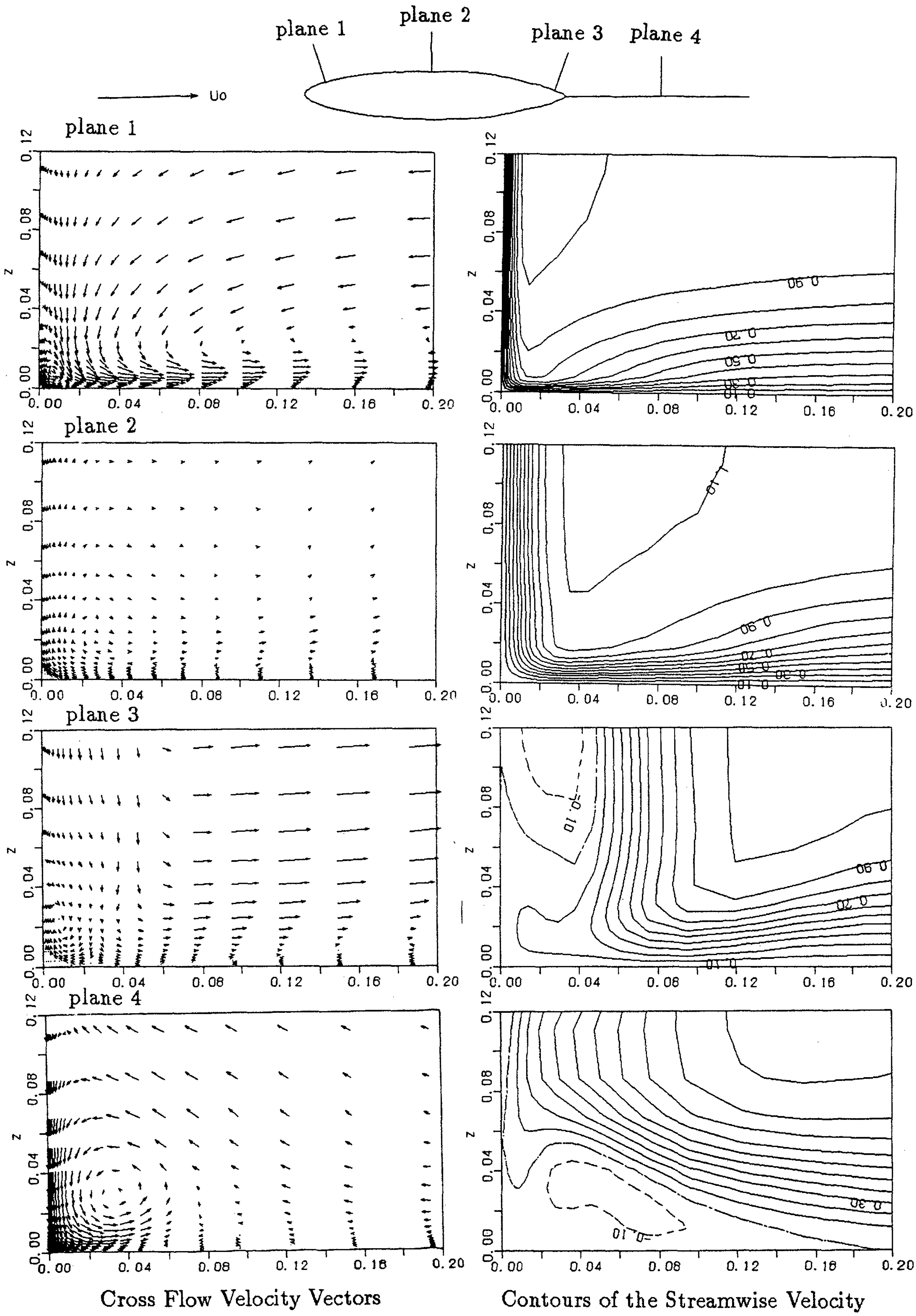

Fig. 9 Cross Flow Velocity Vectors and Contours of the Streamwise Velocity at Several Planes: $R_n = 10^4$, $\alpha = 0°$
(abscissa represents the distance from the strut)

mean the components of the velocities in-plane and normal-to plane respectively here.

The horseshoe vortex generated in the upstream travels down along the strut by changing its direction to streamwise direction. Both the primary and the secondary horseshoe vortices can be clearly seen on the plane 1. Compared with those in the upstream symmetry plane, they become larger in size but weaker in strength and the position moves away off the strut and plate. The streamwise velocity shows a dip-like contour near the juncture. This is due to the momentum transfer from the outflow into the corner region by the horseshoe vortex.

These two vortices dissipate further to be seen hardly on the plane 2. Up to the plane 2 the flow is accelerated around the strut. However the acceleration of the flow near the plate is hindered by the plate, which induces the vertical pressure gradient and upward velocity on the strut. Conversely the deceleration of the flow induces downward velocity on the plane 3. It should be noticed that the vortex on plane 3 is not a secondary horseshoe vortex generated in the upstream but the one generated newly. Here, the separation of the flow can be observed in the upper position of the strut but not close to the root.

A trailing edge vortex can be clearly seen on the plane 4 and a wide separated region can be seen also. This vortex dissipates in the downstream to render a almost boundary layer-like flow at 1.5L downstream from the trailing edge.

In Fig. 10 the limiting velocity on the strut and the velocity on the symmetry plane in the wake are compared between $R_n=10^4$ and 10^3. Strong downward velocities can be seen around the juncture of the leading edge of the strut within the oncoming boundary layer thickness. For $R_n=10^4$, a strong backward flow is observed behind the trailing edge which implies the presence of a z-component of vortex in the wake.

Fig. 11 shows the similar comparison of the pressure. The pressure distribution is 3-dimensional up to a considerable height above the oncoming boundary layer thickness. The pressure is higher near the plate in the fore part of the strut. Sharp changes of the pressure can be seen in the wake plane close to the plate which are due to the vortex in this region. Some wiggles are seen near the trailing edge which may imply that the pressure has not yet been fully converged there.

Fig. 12 shows the contours of the x-component of the skin-friction on the strut. Here, chain lines represent zero-skin-friction lines which may be related with the separation on the strut. They are much affected by the Reynolds number. Compared with the visualized flow (see Fig. 1(b)), the zero-skin-friction lines for $R_n=10^4$ seems to agree well with the observed separation lines.

Fig. 13 shows the limiting velocity vectors on the plate and the velocity on the plane of $z=0.8$ far above the oncoming boundary layer. On the plate, the separation and the attachment points can be seen in front of the leading edge of the strut and velocities are very large within the separated region while the flow is almost two-dimensional on the plane of $z=0.8$.

Fig. 14 shows a similar comparison of the pressure to Fig. 13. The kinks in the pressure on the plate come out due to the horseshoe vortex above the plate. Such kinks cannot be found on the $z=0.8$ plane.

Fig. 15 compares the x-component of the skin-friction on the plate between $R_n=10^4$ and $R_n=10^3$. The negative value of skin friction can be found in front of the leading edge and behind the trailing edge. The region with higher skin friction is closer to the strut for $R_n=10^4$ than for $R_n=10^3$.

Fig. 16 shows the spanwise distribution of the sec-

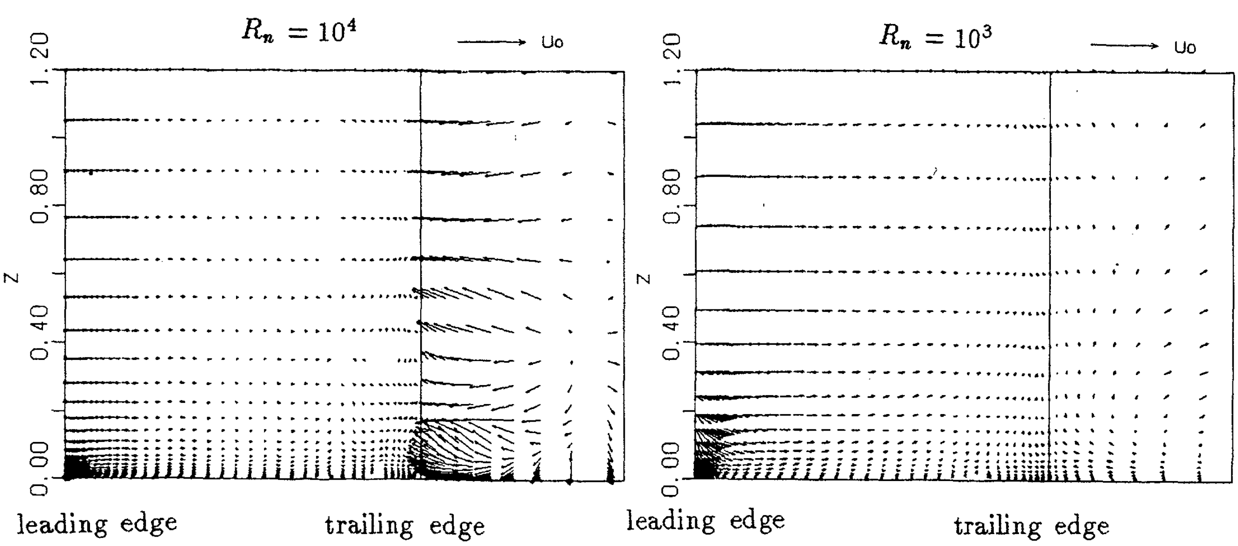

Fig. 10 Velocity Vectors on the Developed Surface of the Strut and Symmetry Plane in the Wake : $\alpha=0°$

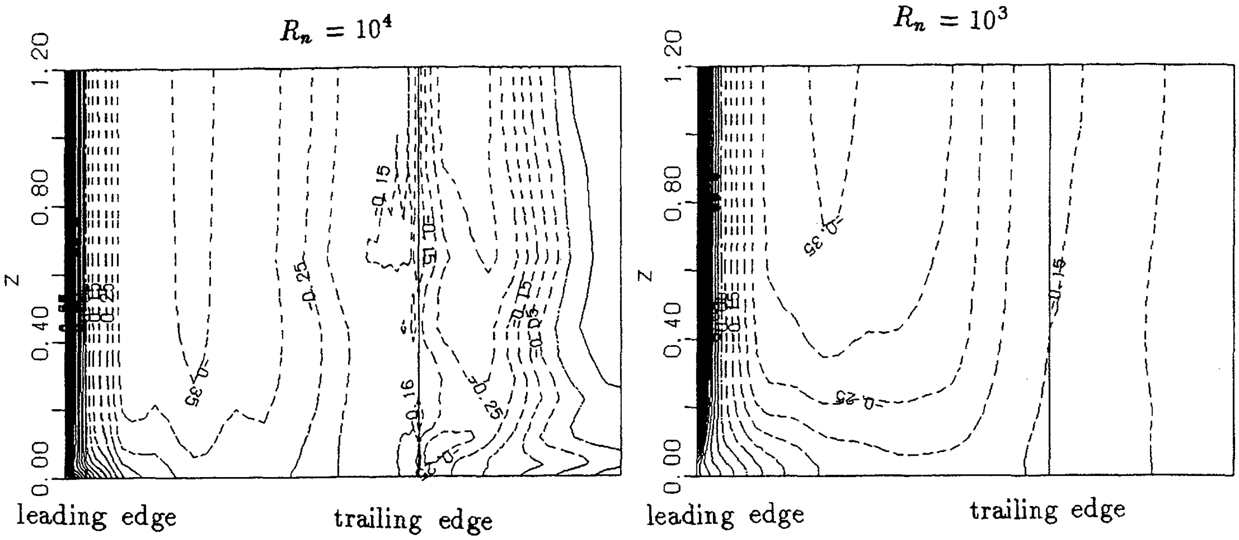

Fig. 11 Pressure on the Developed Surface of the Strut and Symmetry Plane in the wake : $\alpha=0°$

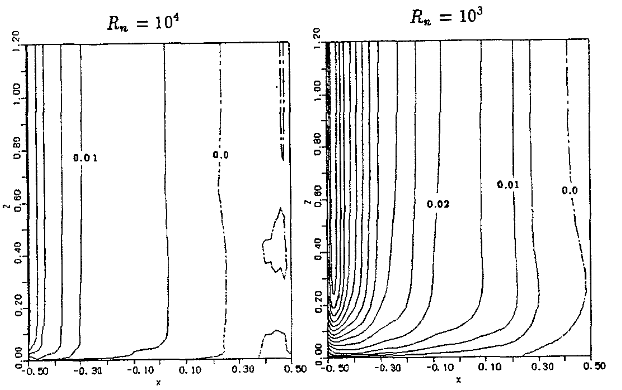

Fig. 12 Distribution of the x-component of the Skin-Friction on the Strut : $\alpha=0°$ (contour interval is 0.005)

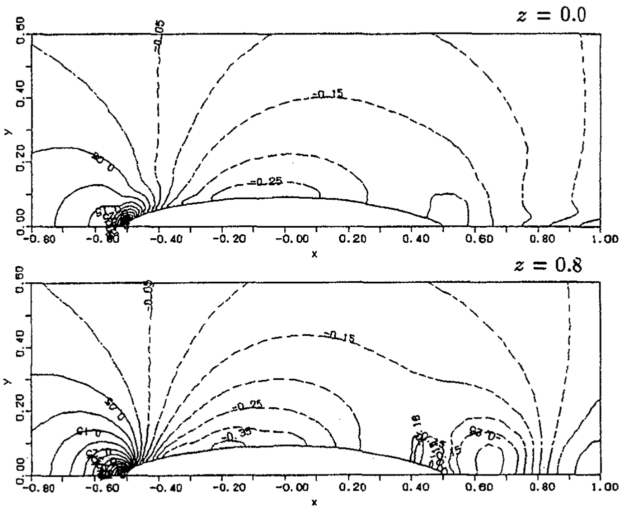

Fig. 14 Comparison of the Pressure between on the Plate and on the Plane $z=0.8$: $\alpha=0°$

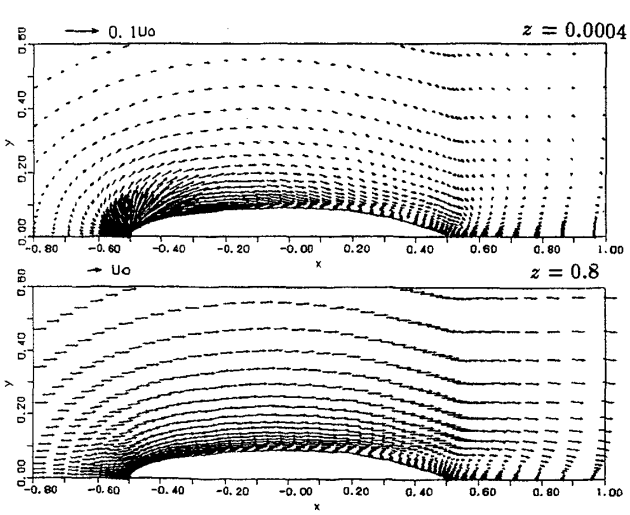

Fig. 13 Comparison of the Velocity Vectors between on the plane $z=0.0004$ and on the plane $z=0.8$: $\alpha=0°$, $R_n=10^4$

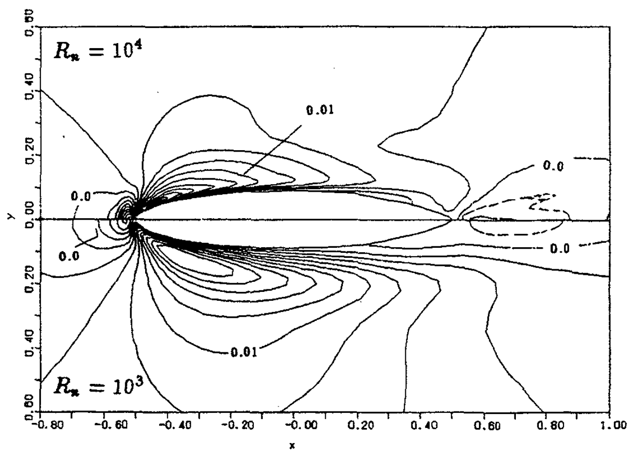

Fig. 15 Comparison of the x-component of the Skin-Friction on the Plate between for $R_n=10^4$ and 10^3 : $\alpha=0°$
(contour interval is 0.002 and broken lines denote negative values)

tional drag coefficients on the strut: for $R_n=10^3$ and $R_n=10^4$. The frictional drag increases within the boundary layer as z increases but is constant above the boundary layer. On the other hand the pressure drag coefficients are much influenced by the distribution of the pressure at the leading edge (see Fig. 6) and separation of the flow at the surface of the strut.

4.2 Junction Flow with Angle of Attack −5°

Fig. 17 shows the flow near the plate. A saddle-point type of separation and nodal point type of attachment can be clearly seen in front of the strut. This flow is similar to the flow with zero angle of attack shown in Fig. 13 but the singular points are shifted toward the pressure side of the strut.

On the suction side, a strong backward flow is seen in the near of the strut and a large scale of vortex is in the wake region but not on the pressure side.

The contour of the x-component of skin friction on the plate is shown in Fig. 18. The zero skin friction lines stretch from the both side of the strut to the downstream. These lines seem to be related with the fish-tail-like line which was found in the experiments of the flow visualization as seen in Fig. 1(a).

Fig. 19 shows the pressure distribution on the plate. The position and direction of the kinks in pressure contour seem to be correlated with the valley of the skin friction contours shown in Fig. 18.

Fig. 20 shows the vorticity contours at several sections to see how vortices are generated and dissipate as the flow goes downstream. All the planes are orthogonal to the strut or wake plane and the normal component of vorticities to the plane are plotted. The behaviour of the horseshoe vortex along the strut is similar to that for the case of zero angle of attack. But the phase of its propagation is in advance in the suction side because the plane where horseshoe vortex is generated is shifted to the pressure side. The trailing vortex can not be seen so clearly because the Reynolds number is small.

Figs. 21 and 22 show the flow and the pressure on the strut and the wake plane. The separation point in the upstream shifts to the pressure side near the plate but it moves toward the leading edge of the strut in proportion to the height. The pressure near the plate hardly change so that the difference of the pressure between the pressure side and the suction side is also small.

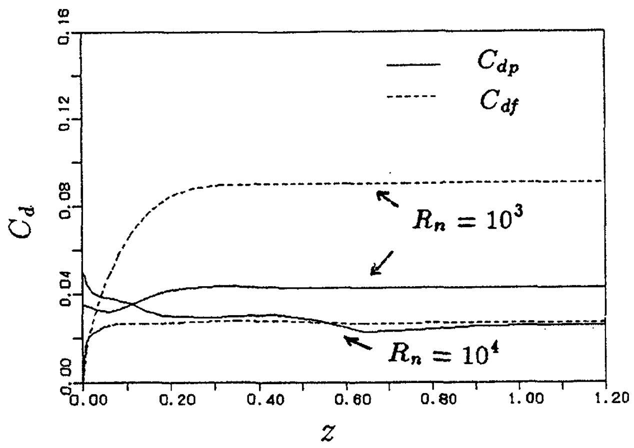

Fig. 16 Spanwise Distribution of the Sectional Drag Coefficients of the Strut: $\alpha=0°$

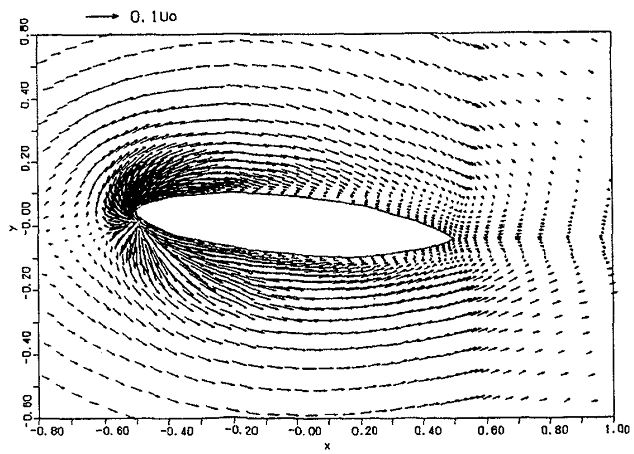

Fig. 17 Limiting Velocity Vectors on the Plate ($z=0.004$): $R_n=10^3$, $\alpha=-5°$

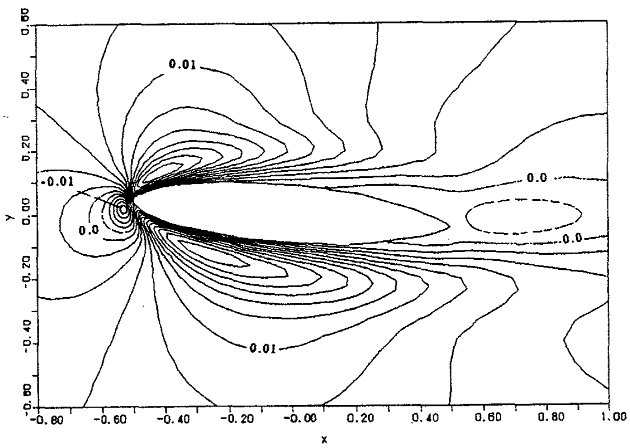

Fig. 18 x-component of the Skin-Friction on the Plate: $R_n=10^3$, $\alpha=-5°$ (contour interval is 0.002 and broken lines denote negative values)

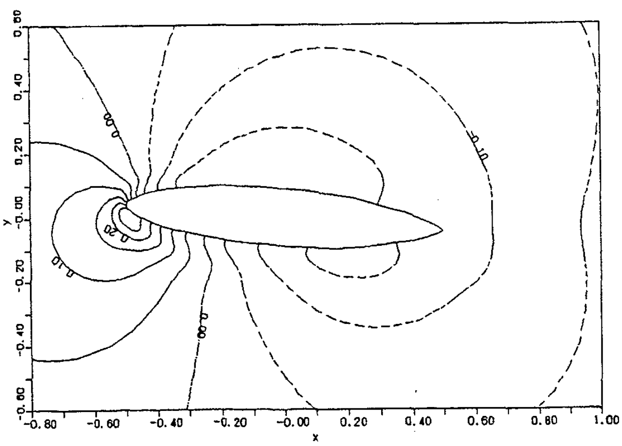

Fig. 19 Pressure on the Plate: $R_n=10^3$, $\alpha=-5°$

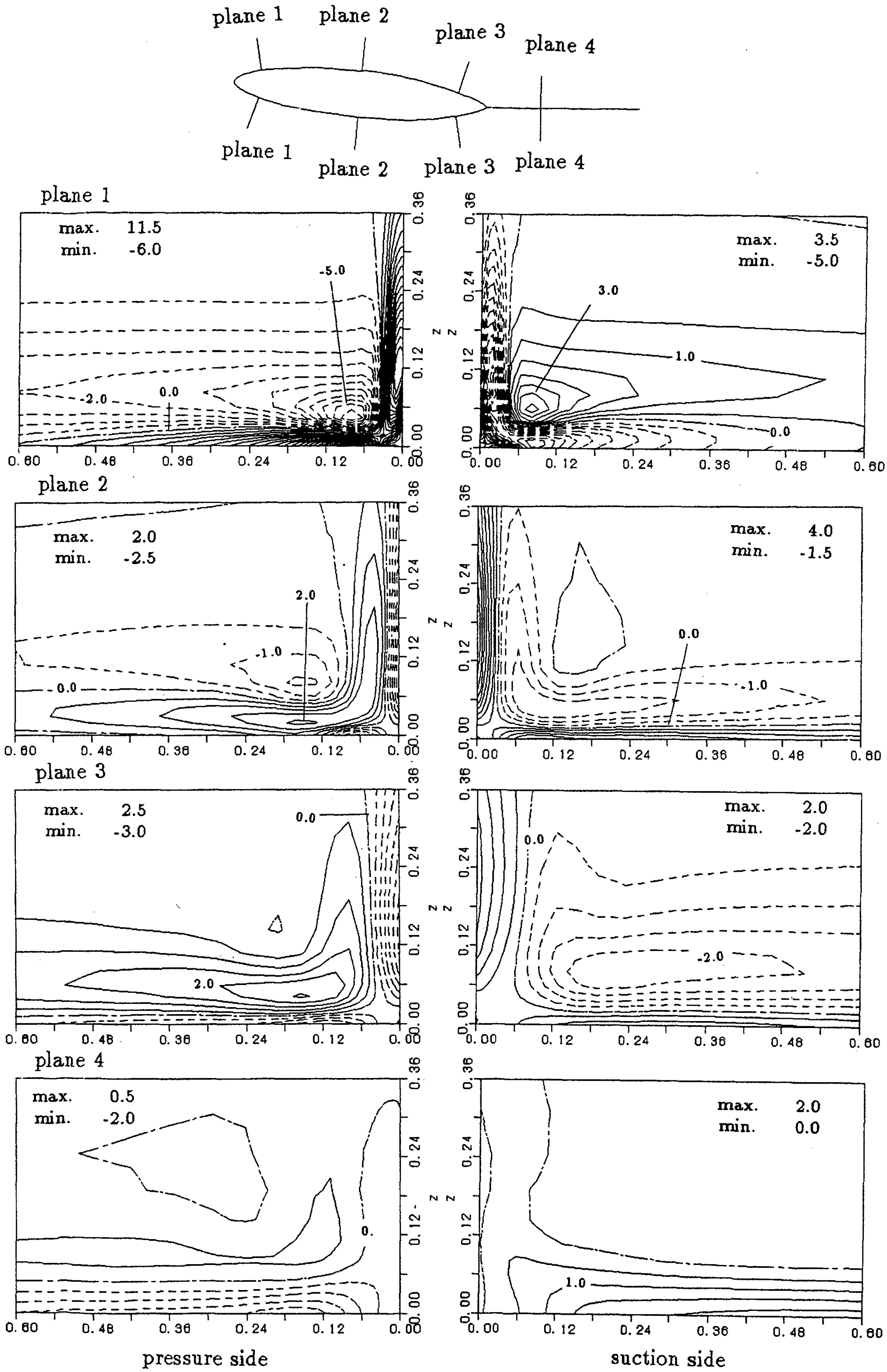

Fig. 20 Vorticity Contours at Several Planes: $R_n=10^3$, $\alpha=-5°$
(contour interval is 0.5 and broken lines denote negative values)

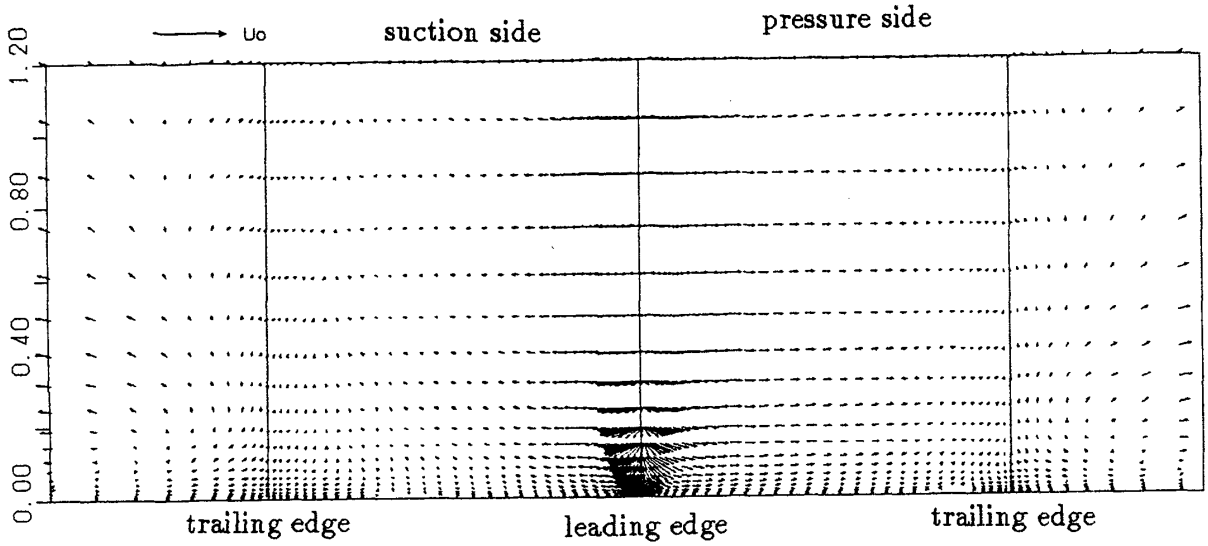

Fig. 21 Velocity Vectors on the Developed Surface of the Strut and wake plane : $R_n=10^3$, $\alpha=-5°$

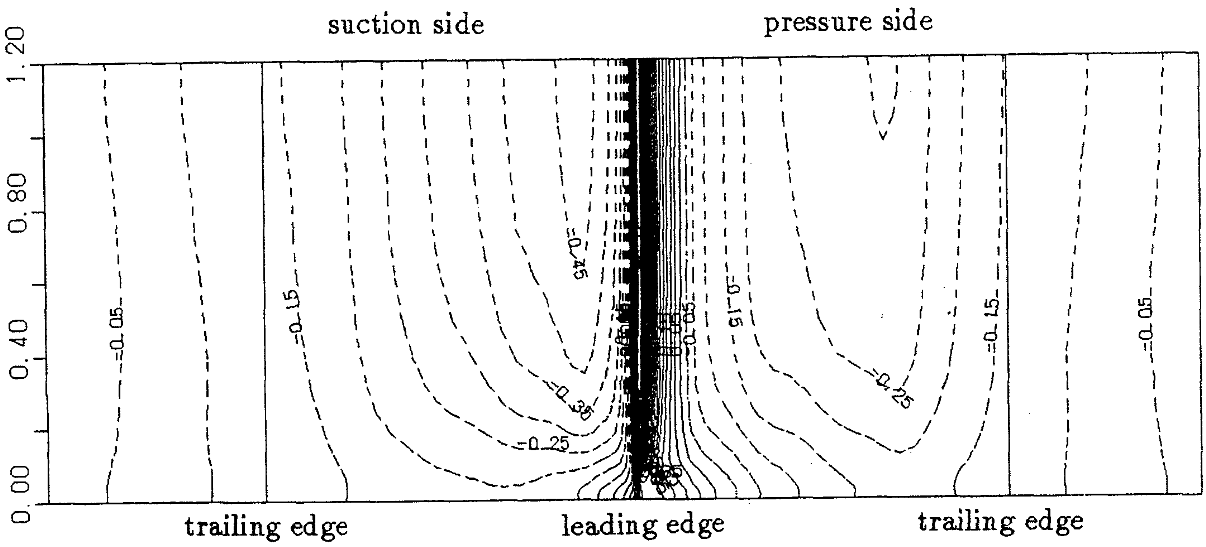

Fig. 22 Pressure on the Developed Surface of the Strut and Wake Plane : $R_n=10^3$, $\alpha=-5°$

Fig. 23 shows the contours of the x-component of the skin-friction on the strut. It can be seen that the separation on the pressure side occures later than that on the suction side. No significance difference is observed in the spanwise distribution of the seperation position from that for zero angle of attack if the Ryenolds number is small. However it differs from the visualization results (shown Fig. 1(c), (d)) whose Reynolds number is about $4*10^4$. The difference is due to the Reynolds number effects.

The spanwise distribution of the drag and the lift coefficients of the strut is shown in Fig. 24. The characteristics of the drag are similar with those for the case with zero angle of attack but the lift is remarkably reduces near the plate due to the insensitive change of pressure there.

5. Conclusions

The junction flow around a strut mounted on a plate with zero and 5° angle of attack has been investigated both by the numerical computation and by the flow visualization to make clear its flow mechanism and drag. The numerical solution obtained by solving the Navier-Stokes equations seems to agree qualitatively with the visualized flow.

The boundary layer flow developed on the plate affects greatly on the flow around the strut. Not only the horseshoe vortex but secondary vortex appear and the separation around the trailing edge show a complicated three-dimensionality. The Reynolds number dependence of the flow is appreciable due to the change of the strength of the horseshoe vortex. The separations

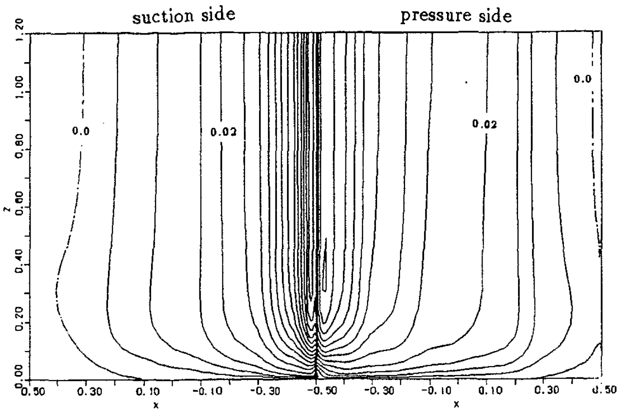

Fig. 23 Distribution of the x-component of the Skin-Friction on the Strut: $\alpha=-5°$ (contour interval is 0.005 and broken lines denote negative values)

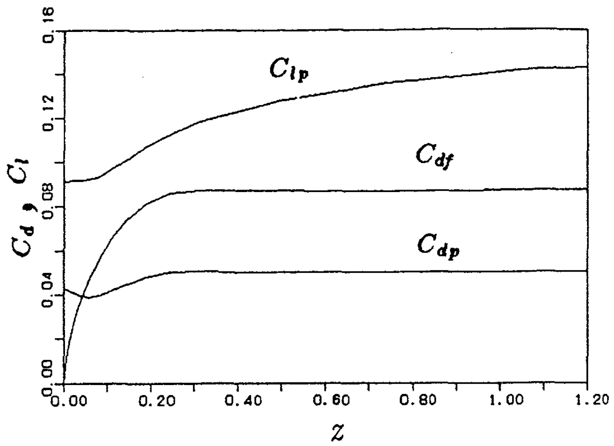

Fig. 24 Spanwise Distribution of the Sectional Drag and Lift Coefficients of the Strut: $\alpha=-5°$

around both the leading and trailing edges are much affected. The pressure and the skin friction acting on the strut varies much in spanwise. The estimation of the drag should be carried out by considering these effects.

The incident angle gives a shift of the horseshoe vortices to the pressure side to make an unsymmetrical structure of the horseshoe vortex in the both sides of the strut but the characteristics of the drag remains little affected.

It can be concluded that a numerical study can be a good tool for such complicated flows. A more general understanding of the junction flow will be made through further studies on the effects of the curvature of the plate and the heel angle of the strut.

The authors expresses their appreciation to Prof. Y. Doi at Hiroshima University for his discussion.

The present research is partially supported by SR213 project of Shipbuilding Research Association of Japan.

References

1) Okamura, N., "Appendage Flows and Forces", 3rd JSPC Symposium on Flows and Forces of Ships, 1989.
2) Ueda, T., Kawakami, Y, "Experimental Studies on Scale effect of Power Estimation Factors and on Hydrodynamic Forces Acting on Bossing of High-speed Container Ship with Twin Screw Propellers", Report of Ship Research Institute, Vol. 17, No. 4, 1980.
3) Baker, C. J., "The Laminar Horseshoe Vortex", J. of Fluid Mechanics, Vol. 95, 1979.
4) Thomas, A. S. W., "The Unsteady Characteristics of Laminar Junction Flow", Physics of Fluids, Vol. 30, 1987.
5) Angui, J., Andreopoulos, J., "Experimental Investigation of a Three-Dimensional Boundary Layer Flow in the Vicinity of an Upright Wall Mounted Cylinder", AIAA 21st Fluid Dynamics, Plasma Dynamics and Laser Conference, 1990.
6) Dickinson S. C., "An Experimental Investigation of Appendage-Flat Plate Junction Flow", DTNSRDC Report DTNSRDCC-86/052, 1986.
7) Devenport, W. J. and Simpson, R. L., "Some Time-Dependent Features of Turbulent Appendage-Body Juncture Flows", 16th Symposium on Naval Hydrodynamics, 1986.
8) Menna, J. D. and Pierce, F. J., "The Mean Flow Structure Around and Within a Turbulent Junction or Horseshoe Vortex-Part 1: The Upstream and Surrounding Three-Dimensional Boundary Layer", J. of Fluid Engineering, Vol. 110, 1988.
9) Pierce, F. J. and Harsh, M. D., "The Mean Flow Structure Around and Within a Turbulent Junction or Horseshoe Vortex-Part 2: The Separated and Junction Vortex Flow", J. of Fluid Engineering, Vol. 110, 1988.
10) Visbal, M. R., "Structure of Laminar Juncture Flows", AIAA J., Vol. 29, No. 8, 1991.
11) Hung, C. M. and Buning, P. G., "Simulation of Blunt-Fin Induced Shock Wave and Turbulent Boundary Layer Interaction", AIAA Paper 84-0457, 1984.
12) Sung, C. H. and Yang, C.-I., "Validation of Turbulent Horseshoe Vortex Flows", 17th Symposium on Naval Hydrodynamics, 1988.
13) Briley, W. R. and McDonald, H., "Three-Dimensional Horseshoe Vortex Flow Using the Navier-Stokes Equations", 7th International Conference on Numerical Methods in Fluid Dynamics, Stanford University and NASA/Ames, 1980.
14) Takamatsu, M., Takebe, T., "Experimental Studies on Junction Flows", Graduate Thesis, Hiroshima Univ., 1992.
15) Welch, J. E., Harlow, F. H., Shannon, J. P. and Daly, B. J., "The MAC Method", Los Alamos Sceintific Laboratory Report LA-3425, Los-Alamos, New-Mexico, 1966.
16) Kwag, S. H., Mori, K. and Shin, M., "Numerical Computation of 3-D Free Surface Flows by N-S Solver and Detection of Sub-breaking", J. of Soceity of Naval Architects of Japan, Vol. 166, 1989.
17) Hoekstra, M., "Recent Developments in a Ship

Stern Flow Prediction Code", 5th International Conference on Numerical Ship Hydrodynamics, Hiroshima, 1989.

18) Kodama, Y., "Three-Dimensional Grid Generation around a Ship Hull Using the Geometrical Method", J. of Soceity of Naval Architects of Japan, Vol. 164, 1988.